

Structures of bimetallic clusters

P. J. Hsu and S. K. Lai^{a)}

Complex Liquids Laboratory, Department of Physics, National Central University, Chungli 320, Taiwan, Republic of China

(Received 18 April 2005; accepted 8 November 2005; published online 30 January 2006)

We report an optimization algorithm for studying bimetallic nanoclusters. The algorithm combines two state-of-the-art methods, the genetic algorithm and the basin hopping approach, widely employed in the literature for predicting structures of pure metallic and nonmetallic clusters. To critically test the present algorithm and its use in determining the lowest-energy structures of bimetallic nanoclusters, we apply it to study the bimetallic clusters $\text{Cu}_n\text{Au}_{38-n}$ ($0 \leq n \leq 38$). It is predicted that the Au atoms, being larger in size than the Cu atoms, prefer to occupy surface sites showing thus the segregating behavior. As the atom fraction of Cu increases, the bimetallic cluster $\text{Cu}_n\text{Au}_{38-n}$, as a whole, first takes on an amorphous structure and is followed by dramatic changes in structure with the Cu atoms revealing hexagonal, then assuming pentagonal, and finally shifting to octahedral symmetry in the Cu-rich range. © 2006 American Institute of Physics.

[DOI: [10.1063/1.2147159](https://doi.org/10.1063/1.2147159)]

I. INTRODUCTION

Bimetallic nanoparticles are important catalysts in fuel cell electrode reactions. To produce this kind of composite material at a lowest cost and yet achieve the best stability and kinetics, it is of industrial interest to be able to monitor the size and composition dependence of particles. Scientifically an understanding of the lowest-energy structure of a bimetallic cluster is a prerequisite to studying its thermal properties. It is the purpose of this work to develop a practically useful algorithm: the parallel tempering multicanonical basin hopping plus genetic algorithm (PTMBHGA), for calculating the lowest-energy geometries of bimetallic clusters. The algorithm starts with the genetic algorithm¹⁻⁴ (GA) and integrates in it the Monte Carlo-based basin hopping^{5,6} (BH) which is applied to all individuals (parents) as well as in the course of generating children. To ensure high stability and reliability of the global energy minimum prediction, two robust modifications on GA are introduced. The first modification is the incorporation of the parallel tempering (PT) technique.^{7,8} It is implemented for improving conformational sampling and for allowing the multiple searching pathway in the potential-energy surface (PES). The second modification is the effort to circumvent the occurrence of “BH barriers” inherent even in BH.

To fully appreciate the salient features of the method, we apply the PTMBHGA to study the structure of bimetallic nanoalloy Cu–Au. This nanoalloy is of particular interest for three reasons. First is that this nanocluster would probably display structural anomalies as implied by its significant deviation from the virtual-crystal approximation.⁹ The second reason comes from the recent density-functional calculations of Rossi *et al.*,¹⁰ who have done an analysis on the structural characteristics of bimetallic clusters Ag–Cu and Ag–Ni in terms of the core-shell chemical ordering and the occurrence

of the polyicosahedral structure arrangement. Their findings point to the possibility of surface segregation in Cu–Au. Finally, there are now available theoretical results,¹¹⁻¹⁵ computer simulations,^{16,17} and experimental data¹⁸⁻²² of Cu–Au clusters which can be consulted for critical evaluation of the present PTMBHGA. Differing from these latter works, our calculations will be confined solely to nanoclusters $\text{Cu}_n\text{Au}_{m-n}$ with the nuclearity $m=38$. We discuss in considerable detail their lowest-energy structures varying as a function of the atom fraction. It will be seen below that the large disparity in size between Cu and Au atoms and the specific nuclearity $m=38$ have the consequence of driving the Cu atoms in $\text{Cu}_n\text{Au}_{38-n}$ to display a dramatic change in structure with declining atom fraction of Cu (unless for reason of clarity hereafter referred to as n). The change begins with the octahedral for $18 \leq n \leq 29$, shows the pentagonal for $13 \leq n \leq 17$, then switches to the hexagonal for $4 \leq n \leq 12$, and finally turns to the amorphous structure for $1 \leq n \leq 3$ when the nanocluster as a whole is viewed. Of particular interest is the structural preference for Au atoms exhibiting the tendency to segregate on the surface of the nanoclusters.

The present work is organized as follows. In the next section, we describe briefly the many-body potential used and proceed to introduce the algorithm proposed in this work. Here, we review the GA, BH, PT, and multicanonical BH (MBH) and give a fair amount of details on how these algorithms are to be integrated leading to the PTMBHGA method. Section III is devoted to numerical results and discussion. We shall present and analyze the variation of the lowest-energy structures of $\text{Cu}_n\text{Au}_{38-n}$ as a function of n and describe how one would systematically classify them into three broad categories. Finally, we summary our main results in Sec. IV.

II. COMPUTATIONAL DETAILS

In this section, we introduce the many-body potential and give documentary details of the GA method, BH tech-

^{a)}Electronic mail: sklai@coll.phy.ncu.edu.tw

nique, and the idea we put forth to combine these two approaches. The PTMBHGA is then applied to calculate the ground-state geometries of $\text{Cu}_n\text{Au}_{38-n}$.

A. Gupta-type potential

To account for the interactions between Cu and Au atoms which are intrinsically many body in nature we employ the widely used n -body Gupta potential.^{23,24} This empirical potential can be written

$$E_n = \sum_{i=1}^n \left\{ \sum_{j=1(j \neq i)}^n A_{ij} \exp\left(-p_{ij}\left(\frac{r_{ij}}{r_{ij}^{(0)}} - 1\right)\right) - \left[\sum_{j=1(j \neq i)}^n \xi_{ij}^2 \exp\left(-2q_{ij}\left(\frac{r_{ij}}{r_{ij}^{(0)}} - 1\right)\right) \right]^{1/2} \right\}, \quad (1)$$

where A_{ij} , ξ_{ij} , p_{ij} , q_{ij} , and $r_{ij}^{(0)}$ are parameters fitted to bulk measured data. There are three sets of parameters of which two sets are homonuclear ($i=j$), one for Cu–Cu and the other for Au–Au, and the third set is heteronuclear ($i \neq j$) for Cu–Au. The former sets are adjusted to bulk data taken from the pure Cu and Au metals and are assumed the same in the nanoalloy; the latter set is determined by fitting to the crystalline structure of an intermetallic compound. In this work, we use the values of the parameters given by Cleri and Rosato.²³ For $i=j$, Cleri and Rosato adjusted separately the heteronuclear parameters to the experimental bulk values of cohesive energy, lattice constant, and elastic constants for the fcc crystal structure at 0 K. For $i \neq j$, they made the same adjustment procedure to the heteronuclear parameters but did the fitting to the fcc-based Cu_3Au structure. Before proceeding further, we should digress for a moment and make a relevant remark on these Gupta-type parameters. In view of the widespread use of Eq. (1) in studies of bulk metals and clusters, there was some effort devoted to choosing the “best” parametric values for this empirical potential form. The detailed analysis was done by Lopez and Jellinek²⁵ using the minimal maximum error fitting scheme (in contrast to the traditional least-squares fitting procedure). These authors illustrated the elegance of the scheme by examining sets of optimized Gupta-type parameters which were uniquely defined by *defining properties*. They then checked the quality of the parameters by their reproducibility of the defining properties and their compatibility in the calculated bulk values compared with those obtained by the usual least-squares fitting scheme. The illustration was done, however, only for the pure nickel metal. Despite their effort, this fitting scheme has not received much attention and certainly has yet to be tested broadly against many other metallic systems. Since the Gupta-type parameters determined by Cleri and Rosato²³ have been applied extensively in the literature for both bulk²⁶ and clusters^{11–14,27} and are generally considered to be reasonable, we have therefore employed below these parametric values.

B. Basin hopping and genetic algorithm methods

The basic idea of the BH method^{5,6} rests on monitoring the PES $E(\mathbf{r}_1, \mathbf{r}_2, \dots, \mathbf{r}_n) \equiv E(\mathbf{X})$ of a finite system of n atoms

and transforming it to a PES $\tilde{E}(\mathbf{X})$ that does not change the global energy minimum nor the relative energies of local minima. In other words, the PES of $E(\mathbf{X})$ is deformed into a multidimensional staircase topography $\tilde{E}(\mathbf{X})$ given by

$$\tilde{E}(\mathbf{X}) = \min[E(\mathbf{X})], \quad (2)$$

where min represents a local-energy minimization for the $E(\mathbf{X})$ of n atoms whose coordinates $\{\mathbf{r}_1, \mathbf{r}_2, \dots, \mathbf{r}_n\}$ are customarily generated randomly. Given the configuration of a cluster and the potential energy calculated by Eq. (1), we can apply the canonical Monte Carlo simulation⁵ to search for the lowest-energy minimum in the deformed PES.

The GA approach begins with a population of parent individuals. A criterion is stipulated and applied to sort out the best individuals (or parents) and discard the remaining ones. Genetic operators are then invoked to generate new individuals (children) for subsequent replacement of the discarded parents. The process is repeated until the best collection of individuals is found and the global energy minimum is presumably contained in this collection.

C. Modified multicanonical Monte Carlo

In preceding sections we outline the GA and BH methods. These methods represent two state-of-the-art techniques widely used in the literature for finding the global energy minimum. The experience gained in applying GA and BH to different kinds of metallic clusters of varying sizes has prompted us to look into the possibility of developing a new algorithm that retains the best features in both algorithms. In this section, we give an account of how we apply the ideas behind the BH and GA to construct a new algorithm called MBH that integrates naturally with GA. To fully enhance the predictive power of the present algorithm, we combine the latter with the PT technique and include many additional features that are quite natural in GA under a parallel computing environment.

The MBH (Ref. 28) is a modification of the Boltzmannian Monte Carlo (MC) scheme. In essence it focuses on the multidimensional staircase topography $\tilde{E}(\mathbf{X})$ defined in Eq. (2). In terms of $\tilde{E}(\mathbf{X})$, the non-Boltzmann multicanonical weight factor is given by

$$w_{mu}(\tilde{E}) = e^{-\beta^{mu}(\tilde{E})\tilde{E} - \alpha^{mu}(\tilde{E})}, \quad (3)$$

where $\beta^{mu}(\tilde{E})$ is an effective inverse temperature and $\alpha^{mu}(\tilde{E})$ is a multicanonical parameter. Since w_{mu} depends on $\beta^{mu}(\tilde{E})$ and $\alpha^{mu}(\tilde{E})$, it is *a priori* unknown. It can, however, be determined iteratively as follows. First, we carry out a BH run (recursion step) using initial values $\beta^{mu}(\tilde{E}) = \hat{\beta}_0$ (to be given below) and $\alpha^{mu}(\tilde{E}) = 0$ to construct a histogram of the energy distribution $H(\tilde{E})$. The value \tilde{E} is confined to the range $E_{\min} \leq \tilde{E} \leq E_{\max}$, where E_{\min} and E_{\max} are, respectively, the lower and upper limits of energies. The latter can be estimated from either running GA or a single-canonical BH following the methods detailed in Secs. II B and II C of Ref. 29,

respectively. By appealing to $H(\tilde{E})$ and initializing $S(\tilde{E})=0$, we may calculate the entropy array $S(\tilde{E})$ by $S(\tilde{E})=S(\tilde{E}) + \ln H(\tilde{E})$. The multicanonical parameters can now be obtained in two consecutive steps,

$$\beta^{mu}(\tilde{E}) = \begin{cases} \hat{\beta}_0, & \tilde{E} \geq E_{\max} \\ \hat{\beta}_0 + [S(\tilde{E}') - S(\tilde{E})]/(\tilde{E}' - \tilde{E}), & E_{\min} \leq \tilde{E} < \tilde{E}' < E_{\max} \\ \beta^{mu}(E_{\min}), & \tilde{E} < E_{\min} \end{cases} \quad (4)$$

and

$$\alpha^{mu}(\tilde{E}) = \begin{cases} \alpha^{mu}(\tilde{E}') + [\beta^{mu}(\tilde{E}') - \beta^{mu}(\tilde{E})]\tilde{E}', & \tilde{E} < E_{\max} \\ 0, & \tilde{E} \geq E_{\max}, \end{cases} \quad (5)$$

where \tilde{E} and $\tilde{E}' = \tilde{E} + \delta\tilde{E}$ in Eqs. (4) and (5) are adjacent bins of the array $S(\tilde{E})$. Next, these initial set of values $\beta^{mu}(\tilde{E})$ and $\alpha^{mu}(\tilde{E})$ are employed in Eq. (3) and another recursion step is performed to produce a new set of $\beta^{mu}(\tilde{E})$ and $\alpha^{mu}(\tilde{E})$. The procedure is repeated until a desired w_{mu} appears. Recall that the probability distribution function of an energy state \tilde{E} in the canonical MC is given by

$$P_B(T, \tilde{E}) \propto g(\tilde{E})w_B(\tilde{E}) \equiv g(\tilde{E})e^{-\tilde{E}/(k_B T)}, \quad (6)$$

where $g(\tilde{E})$ is the density of states and $w_B(\tilde{E})$ is the Boltzmann weight factor. This expression for P_B differs from the usual MC in that the energy state is the deformed \tilde{E} . Now, in MBH, we define another energy distribution function

$$P_{mu}(\tilde{E}) \propto g(\tilde{E})w_{mu}(\tilde{E}). \quad (7)$$

The desired w_{mu} mentioned above is the one iterated until $P_{mu}(\tilde{E})$ is a constant. Accordingly, $g(\tilde{E}) \propto w_{mu}^{-1}(\tilde{E})$ and we arrive at a relation between P_B and P_{mu} as

$$P_B(T, \tilde{E}) \propto P_{mu}(\tilde{E})w_{mu}^{-1}e^{-\tilde{E}/(k_B T)}, \quad (8)$$

which is the energy distribution function to be used for effecting the canonical ensemble average of a physical quantity.

D. Parallel tempering method

We turn now to the PT technique. This technique is introduced as a means to extend further the configurational search space. Here it suffices to recall the main idea behind this approach. Let us consider a configuration, say C_i . Subject to some prescribed condition, C_i is replaced by C_{new} . A Metropolis criterion is applied to check on $\min(1, e^{-\Delta E_i \beta_i^{PT}})$, where $\beta_i^{PT} = 1/(k_B T_i^{PT})$ is the i th PT inverse temperature and $\Delta E_i = E(C_{new}) - E(C_i)$. In other words, for any two configurations C_i and C_j , one may effect a temperature change from (C_i, T_i^{PT}) to (C_j, T_j^{PT}) by implementing the Metropolis criteria $\min(1, e^{-\Delta E_i \beta_i^{PT}})$ and $\min(1, e^{-\Delta E_j \beta_j^{PT}})$. Note that the PT technique is naturally included into GA in the course of generating different C_{new} for children.

E. Parallel tempering multicanonical basin hopping plus genetic algorithm

The stage is now ready to describe PTMBHGA. To begin with, we consider N individuals (taken to be 20 in this work) each of which is generated randomly with atoms arranged in an unbiased initial state C_i , $i=1, 2, \dots, N$. Given an initial $\hat{\beta}_0$ which is set equal to $1/1000 \text{ K}^{-1}$ ($k_B=1$), we perform MBH separately for all individuals and locate their minimized energy values. These are done in the present work by the MPI parallel computing. The lowest energies as well as the multicanonical parameters are recorded and stored for subsequent use. Next, we prepare N evenly spaced parallel tempering parameters, namely, $\beta_1^{PT}=12.5, \dots, \beta_N^{PT}=1.25$ (inverse temperature in reduced units).³⁰ These parameters β^{PT} are assigned to individuals, each with one β^{PT} , for the purpose of implementing PT. To proceed further, we treat the “energy-minimized” individuals as parents and calculate their fitness using Eq. (5) of Ref. 29. This information on the fitness of all individuals is utilized as a criterion to discard 25% of the parents, and the remaining parents are used to generate children (and hence recover the discarded parents) by the operation of genetic operators. The PT is at this point implemented as follows. First we generate a random number ν ($0 < \nu < 1$) and scan the sorting parameter $\phi_i = \sum_{j=1}^i f_j$, where $f_1 > f_2 > \dots > f_{15}$ are the fitness (of the best 75% parents) in sequence of ϕ_1, ϕ_2, \dots , until the specific condition $\phi_i > \nu$ is met. The parent to be selected for the child generation is then the i th parent which will proceed to MBH run with the preassigned PT parameter β_i^{PT} . As a concrete illustration, suppose we apply the arithmetic operator to produce one child with the configuration $C_{new} = (C_i + C_j)/2 = \{(x_1 + y_1)/2, (x_2 + y_2)/2, \dots, (x_{3n} + y_{3n})/2\}$ from two parents, ϕ_i and ϕ_j , whose configurations are $C_i = \{x_1, x_2, \dots, x_{3n}\}$ and $C_j = \{y_1, y_2, \dots, y_{3n}\}$. A local-energy minimization for the child’s energy at C_{new} is then performed. Next, we calculate two transition probabilities,

$$P(\tilde{E}(C_i) \rightarrow \tilde{E}(C_{new})) = e^{-\beta_i^{PT}[\tilde{E}(C_{new}) - \tilde{E}(C_i)]}, \quad (9)$$

$$P(\tilde{E}(C_j) \rightarrow \tilde{E}(C_{new})) = e^{-\beta_j^{PT}[\tilde{E}(C_{new}) - \tilde{E}(C_j)]}, \quad (10)$$

for the two parents C_i and C_j . A decision on which probability to keep is then made by checking the Metropolis criteria. If neither [or only one of $P(\tilde{E}(C_i))$ and $P(\tilde{E}(C_j))$] probability is accepted, we discard (retain) the C_{new} . On the other hand, if both probabilities are accepted, we choose the one with the higher fitness. This PT procedure is applied to each genera-

TABLE I. Gupta-type potential parameters for the bimetallic cluster Cu–Au taken from Cleri and Rosato (Ref. 23). $r_{ij}^{(0)}$ is scaled by the Bohr radius.

ij	A_{ij} (eV)	ξ_{ij} (eV)	p_{ij}	q_{ij}	$r_{ij}^{(0)}$
Cu–Cu	0.0855	1.2240	10.960	2.2780	2.556
Cu–Au	0.1539	1.5605	11.050	3.0475	2.556
Au–Au	0.2061	1.7900	10.229	4.0360	2.884

tion of a child and is continued until the 25% discarded parents have been successfully refilled. We should remark at this point that the original BH method is actually a modified canonical MC method with only the local-energy minima sorted for the lowest energy. As in the canonical MC method, it assumes also a Boltzmann factor form which, though it can be adjusted dynamically by following closely the acceptance ratio in the simulation, is fixed throughout at its effective temperature. We remark furthermore on two technical modifications. The first one is to apply the MBH (instead of BH) for a reasonable number of recursion steps. This modification is done in an attempt to reduce the chance of the system being trapped by BH barriers. The second modification is to introduce a PT technique which, via the various weight factors β_i^{PT} , allows a multiple searching pathway in the PES. The technique is equivalent to operating several independent “MC machines” that run MBH simultaneously. For each machine, it uses its own β_i^{PT} parameter to calculate the transition probability and, in the course of generating children, exchanges information between individuals on both the coordinates and temperatures. We thus see that the use of multicanonical weight factors is an important strategy here. With the latter forming the backbone of parents which is further enhanced by the PT technique, it is possible to jump over a very large-scaled energy barrier. As far as the Markov chain rule is concerned, the use of genetic operators to generate new configurations may be a good substitution for the traditional Monte Carlo random move. The complete flow charts of the PTMBHGA method and the technical details of MBH are available on request.

III. NUMERICAL RESULTS AND DISCUSSION

A. Bimetallic clusters Cu–Au

We have applied the PTMBHGA method to calculate the lowest-energy structures of $\text{Cu}_n\text{Au}_{38-n}$ (hereafter denoted by C_n) for $n=0$ (Au_{38}), \dots , 38 (Cu_{38}). Table I gives the Gupta potential parameters used. These values were taken from Cleri and Rosato.²³ The optimization results were carried out as follows. For all individuals, we ran PT *multicanonical* BH for 30 recursion steps and, in each recursion step, performed 100 BH steps [Eq. (3)]. Next, we applied 30 recursion steps for subsequent generations of children in GA and, in each generation of a child and in each recursion step, repeated 50 BH steps.³¹ In the present approach, we have introduced a new genetic operator in GA. It consists of effecting a permutation on each pair of atoms of different types for any randomly selected parent. This permutation action can be considered also as some kind of a random-move method. Our experience shows that this permutation process effected on

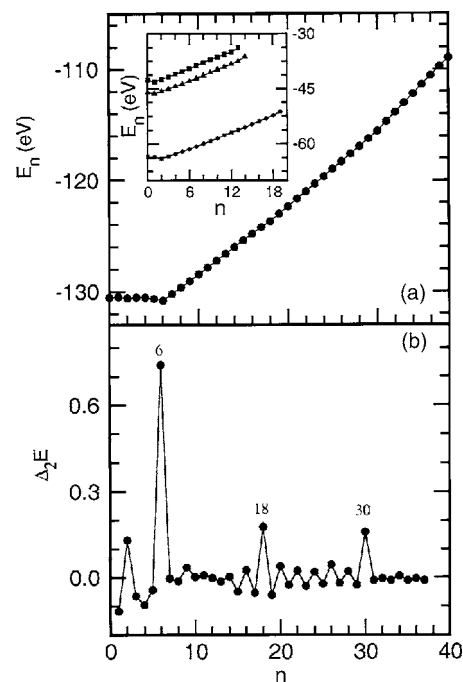


FIG. 1. (a) Total potential energy E_n vs n (atom fraction of Cu) and (b) second energy difference Δ_2E vs n for bimetallic clusters $\text{Cu}_n\text{Au}_{38-n}$ calculated using PTMBHGA. Notations for the insert in (a) (see text) are $m=13$, solid squares (top); $m=14$, solid triangles (middle); $m=19$, stars (bottom).

subsequent generations of children generally yields a better search of energy minima for bimetallic clusters. For the purpose of cross checking the optimized results, we have performed separately for a few randomly chosen bimetallic clusters a PT *single-canonical* BH using 1000 BH steps for each of the 20 individuals before the first generation in GA. Then, in the next step, we locate the lowest-energy value by carrying out 10 000 generations. We refer the interested reader to Fig. 2 of our previous work²⁹ for the detailed numerical procedure of the single-canonical BH. In Fig. 1(a), we plot the lowest-energy minimum E_n vs n and depict, in Fig. 1(b), the second energy difference $\Delta_2E = E_{C_{n+1}} + E_{C_{n-1}} - 2E_{C_n}$ presented as a means to check the relative stability of clusters. It is interesting to see that the minimized energy E_n of C_n weakly decreases with increasing n and achieves a distinctly lowest energy at $n=6$ beyond which E_n increases. Below we analyze the structures C_n at the lowest-energy states. They are classified into three main categories. Let us take a closer look at these sets of representative clusters.

The first category, to which bimetallic clusters $C_{18 \leq n \leq 38}$ belong, is characterized by all C_n assuming the usual truncated octahedron O_h , which is the same geometry as those predicted for the pure clusters K and Rb of size 38.²⁹ For this series of clusters, depicted in Figs. 2(a) and 2(b), a general scenario is that the Au atoms that substitute for the host Cu atoms tend to distribute themselves on the surface. If the cluster is rotated to an orientation showing four Cu atoms forming a square face and arranged one set each on the top and bottom [see Fig. 2(a) for pure Cu], the structural change of the cluster as a function of n can be described in two sequences. The first sequence [Fig. 2(a)], comprising clusters $C_{30 \leq n \leq 37}$, proceeds by replacing the Cu atom at the center of

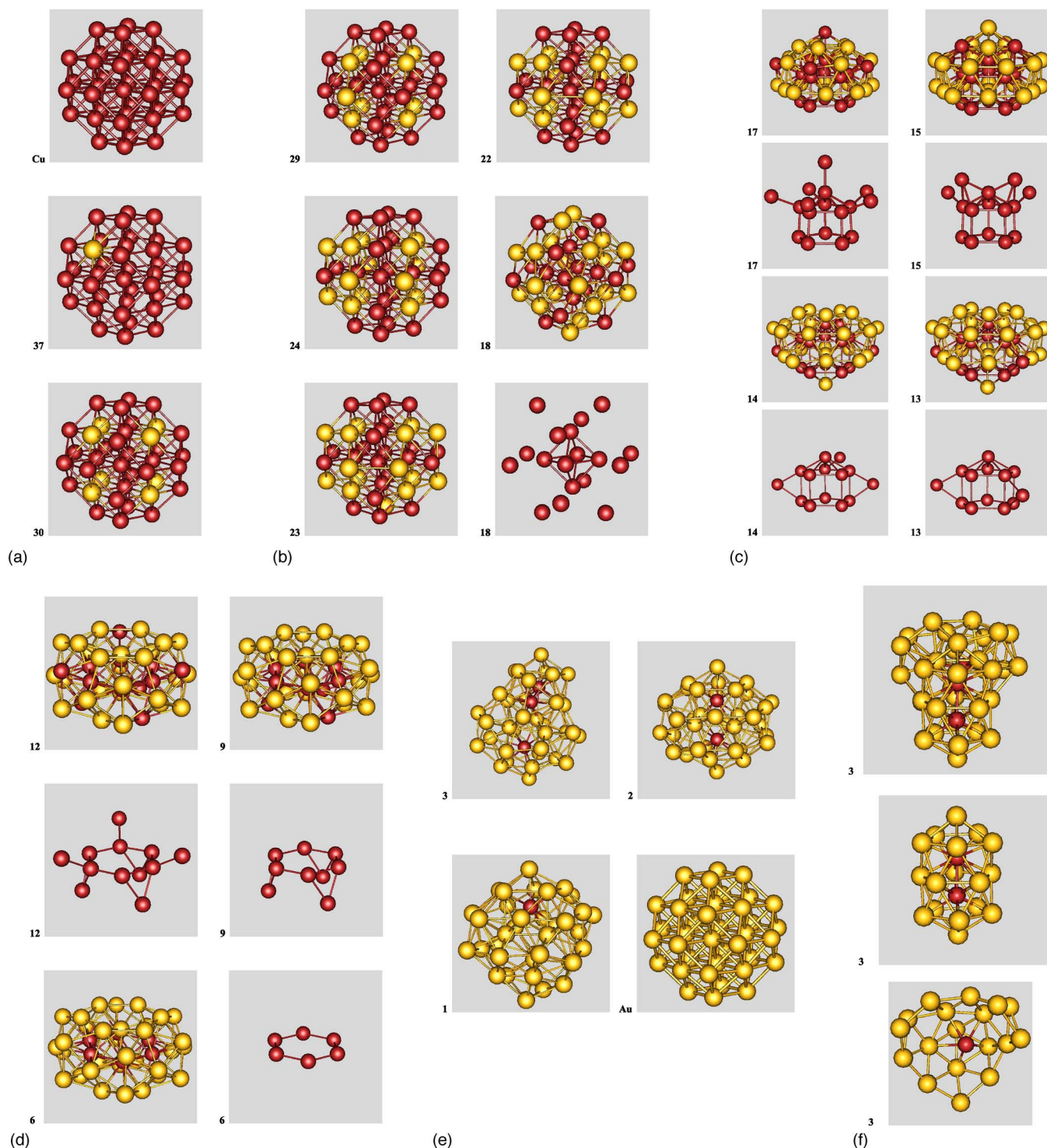


FIG. 2. (Color online) (a) Lowest-lying isomers for pure Cu (top), C_{37} (middle), and C_{30} (bottom). (b) Lowest-lying isomers C_n for $n=29, 24, 23, 22$, and 18 . The Cu atoms in C_{18} are isolated to show the octahedron embedded inside the cluster. (c) Lowest-lying isomers C_n for $n=17$ and 15 – 13 . The Cu atoms in C_{17} and C_{15} – C_{13} are isolated to show the pentagonal symmetry embedded inside the cluster. (d) Lowest-lying isomers C_n for $n=12, 9$, and 6 . The Cu atoms in C_{12}, C_9 , and C_6 are isolated to show the hexagonal symmetry embedded inside the cluster. (e) Lowest-lying isomers for the pure cluster Au and C_n for $n=3, 2$, and 1 . The Cu atoms in C_3, C_2 , and C_1 are embedded inside the disordered distribution of Au atoms. (f) Lowest-lying isomer for C_3 . The geometry of C_3 derives from a double icosahedral (middle) and an amorphous (bottom) structures. Red: Cu and Yellow: Au.

the hexagonal face in C_{38} with a Au atom yielding the cluster C_{37} . The same geometrical replacement continues until all eight Au atoms are so positioned. The sequence terminates at the most symmetrical C_{30} . As n (<30) decreases, we come to the second sequence $C_{18 \leq n \leq 29}$ displayed in Fig. 2(b). Here we note that the square faces (and hence the hexagonal faces

as well) of the O_h symmetry gradually distort to rhombic faces as n decreases. It is noticeable, in particular, that for the lower n clusters $C_{n < 23}$, these rhombic planes are seen to twist dihedrally. The reason for the geometrical change can be traced to the less symmetrical substitution of the Cu atoms at the corner sites of the hexagonal surfaces by larger-

sized Au atoms. In fact, for clusters in the range $24 \leq n \leq 29$, the evolution of C_n is considered regular—the Au atoms are found to reside solely on the central belt region. An exceptional case occurs for the cluster C_{23} because one Cu atom in the top (or bottom) face has been replaced by a Au atom. The same central belt distribution of Au atoms is recovered, however, at $n=22$. At lower still atom fraction of Cu, $18 \leq n < 22$, the remaining bimetallic clusters are manifested by the Au atoms replacing the Cu atoms that occupy the top and bottom rhombic faces. It should be pointed out that despite these structural differences, there is nevertheless one feature common to all $C_{18 \leq n \leq 37}$, namely, an octahedron is always found inside at the center of the cluster.

Now, from our recent studies of the pure alkali metallic clusters [see Fig. 3 of Ref. 29 for Δ_2E], a truncated octahedron in which a distorted rhombus appears would generally signal an energetically less stable cluster (such as those pure clusters Na and Cs of size 38). It is therefore of interest to delve further into the structural stability of this kind of cluster. A useful indicator of the relative stability of a cluster is provided by Δ_2E . Figure 1(b) shows that C_{18} is one of the two relatively more stable structures among the truncated octahedron series. Apparently, the structure of C_{18} appears to be not in accordance with that of pure clusters. It would therefore be worthwhile to seek another piece of evidence useful for shedding light on the stability of a cluster. To this end, we recall a recent work of Rossi *et al.*,¹⁰ who proposed examining the subtle competition between the internal strain and the maximization of the bond number among the constituent atoms in a nanoalloy. Since nanoclusters in this category have the same O_h symmetry, it is instructive to compare first the interatomic distances $r_{\text{Cu-Au}}$ in C_n and $r_{\text{Cu-Cu}}$ in pure clusters. Let us start with $C_{37 \geq n \geq 30}$ focusing in the first place on C_{37} . The Au atoms sit on the surface at the eight centers of the hexagonal faces originally occupied by Cu atoms. The distance between a Au atom, labeled as A, and one internal (surface) Cu atom, labeled as B (C), is $r_{\text{Au-Cu}}^{A-B} = 2.5657 \text{ \AA}$ ($r_{\text{Au-Cu}}^{A-C} = 2.5034 \text{ \AA}$) (see Fig. 3), whereas that of the pure cluster Cu calculated at the same geometrical position is $r_{\text{Cu-Cu}}^{A-B} = 2.5429 \text{ \AA}$ ($r_{\text{Cu-Cu}}^{A-C} = 2.5018 \text{ \AA}$). Since the bond lengths of Cu–Cu and Au–Au are different [see Table I for $r_{ij}^{(0)}$], the replacement of a Cu atom in C_{38} by a Au atom with larger $r_{\text{Au-Au}}^{(0)}$ (Table I) generally can lead to an inherent strain if the Au atom is found inside the cluster. The fact that the larger size Au atom prefers to lie on the surface somehow allows this inherent strain to be efficiently relieved and in the present situation yields a mixed structure. A measure of the latter can be deduced from calculating the average distance of a Au atom from the center of the cluster by the simple formula,

$$\langle R_i \rangle = \frac{1}{n_i} \sum_{i=1}^{n_i} \sqrt{x_i^2 + y_i^2 + z_i^2},$$

where $n_i = n_{\text{Au}}$ is the number of Au atoms in C_n and for $C_{37 \geq n \geq 30}$, $8 \geq n_{\text{Au}} \geq 1$. Since Au atoms in this Au-poor range occupy symmetrical sites [Fig. 2(a)], we expect the $\langle R_i \rangle$ results for $n_{\text{Au}} = 1, \dots, 8$ to be nearly the same, the results are indeed shown in Fig. 4. For comparison we present also in

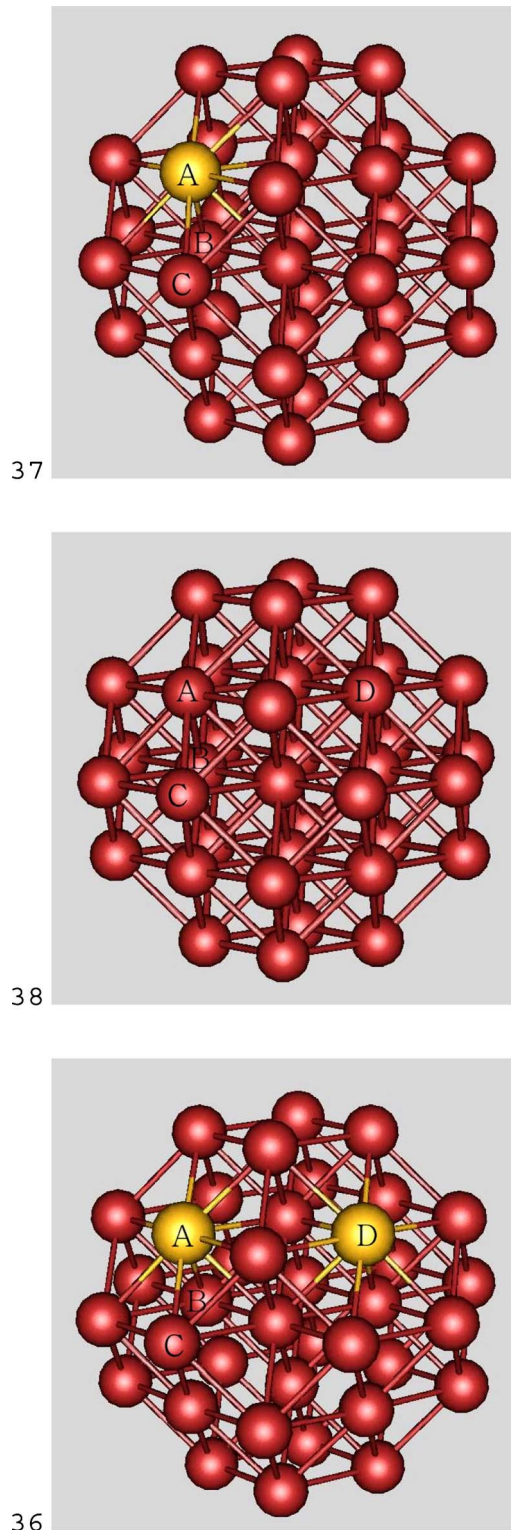


FIG. 3. (Color online) Lowest-lying isomers C_n for $n=38$ (middle), 37 (top), and 36 (bottom). Atoms at the surface sites are labeled by A (top) or A and D (bottom) to be compared with the atoms located at the same positions for the pure cluster Cu (middle). The atom that lies inside in each C_n is labeled by B. Red: Cu and Yellow: Au.

the same figure the results for the remaining $n_{\text{Au}} > 9$ as well as $\langle R_{\text{Cu}} \rangle$ for C_n . As so defined, $\langle R_i \rangle$ describes the degree of mixing within the cluster. A small (large) $\langle R_i \rangle$ value indicates a segregated cluster with the i th type atoms locating at the center (surface) of the cluster and values lying in between

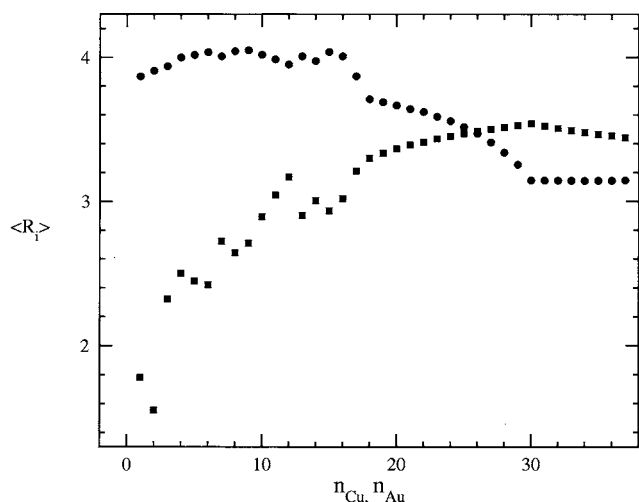


FIG. 4. Order parameter $\langle R_i \rangle$ vs n_{Cu} or n_{Au} giving a measure of the degree of mixing for the average distance from the center of the cluster of an i th atom in n_i of C_n (see text). Notations used: Cu, squares; Au, circles.

signaling a well-mixed cluster. In the Au-poor range ($30 \leq n \leq 37$), the general trend for $\langle R_{\text{Au}} \rangle$ as mentioned above is that they virtually stay constant and are relatively large in magnitude, a result indicating the preference of Au atoms to reside on the surface. Note that $\langle R_{\text{Au}} \rangle$ of $C_{37 \geq n \geq 30}$ are relatively smaller compared with those $\langle R_{\text{Au}} \rangle$ of $C_{n < 30}$, whose values increase stepwise (Fig. 4). This variation in $\langle R_{\text{Au}} \rangle$ points to the tendency of Au atoms to be distributed at sites away from the center of cluster. We should emphasize furthermore that the predicted $C_{37 \leq n \leq 30}$ are energetically stable; for the changes in cluster cohesive energy on mixing defined by¹³

$$\Delta E_{\text{mix}} = E_n - \frac{n}{38} E_{38}^{\text{Cu}} - \frac{n_{\text{Au}}}{38} E_{38}^{\text{Au}},$$

where E_n is given by Eq. (1) and E_{38}^{Cu} (E_{38}^{Au}) is the cohesive energy of the pure Cu (Au) cluster, are all found to be negative (Fig. 5). These clusters are therefore thermodynamically stable. With these $\langle R_i \rangle$ and ΔE_{mix} features in mind, it is then

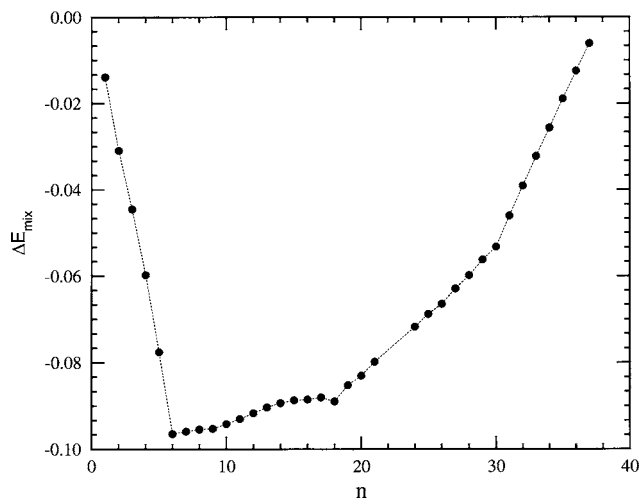


FIG. 5. Energy of mixing ΔE_{mix} vs n (atom fraction of Cu) describing the change in cluster cohesive energy on mixing.

not unexpected to see the structural characteristic of Au atoms in C_{36} , which shows (see Fig. 3) the interatomic distances $r_{\text{Au-Cu}}^{A-B}$ and $r_{\text{Au-Cu}}^{A-C}$ increasing to 2.5666 and 2.5042 Å, respectively. For this nanoalloy, we may compare also $r_{\text{Au-Au}}^{A-D} = 3.6290$ Å with its counterpart for pure cluster of Cu, $r_{\text{Cu-Cu}}^{A-D} = 3.5958$ Å. It thus appears that the Au atoms, given a choice, would very much likely to occupy sites on the surface. Doing so would help maintain a larger separation between Cu and Au atoms (hence minimizing the internal strain) while at the same time optimizing the bond length between atoms on the surface. A stabilized cluster structure is therefore possible if the surrounding Au atoms are so arranged to meet this condition. A reduction in the internal strain is probably the main cause for the relatively stable structure of C_{18} .

Turning to the second category, we investigate C_n covering the range from $n=17$ to 4. As shown in Figs. 2(c) and 2(d), this cluster series is dominated by Au-rich atoms whose larger physical size has played quite a different role. This can be seen by scrutinizing again $\langle R_{\text{Au}} \rangle$ (Fig. 4). Notice that $\langle R_{\text{Au}} \rangle$ increases roughly stepwise, with a distinctive n dependence in each of three ranges of n , namely, $37 \geq n \geq 30$, $30 > n \geq 18$, and $17 \geq n \geq 1$. Since Au atoms in the range $37 \geq n \geq 30$ lie on the surface, the next two plateaus whose $\langle R_{\text{Au}} \rangle$ magnitudes are even larger should describe clusters either well mixed or segregated with Au atoms away from the center of clusters. On the other hand, the $\langle R_{\text{Cu}} \rangle$ of Cu atoms remain nearly constant for $37 \geq n \geq 26$, gradually decreasing for $26 > n \geq 18$, and declining rapidly from $n=17$ thereon. The latter result indicates that the Cu atoms in the Cu-poor range have a greater tendency to segregate at the center of clusters. To find out whether a cluster is in a segregating or mixing state, a further piece of evidence is perhaps useful. Following Wilson and Johnston,¹³ we calculate the order parameter

$$O_{\text{NN}} = \frac{\sum_{i=1}^{n_{\text{Au}}} \sum_{j=n_{\text{Au}}+1}^{38} \delta_{ij}}{\sum_{i=1}^{37} \sum_{j=i+1}^{38} \delta_{ij}},$$

where

$$\delta_{ij} = \begin{cases} 1, & r_{ij} \leq 1.2r_{\text{NN}} \\ 0, & r_{ij} > 1.2r_{\text{NN}} \end{cases}$$

is defined to be the number of Au–Cu nearest-neighbor (NN) interactions relative to the total number of nearest-neighbor interactions. In the above equations, the nearest-neighbor distance r_{NN} is taken to be $r_{ij}^{(0)}$,¹³ whose numerical values are listed in Table I. The so defined O_{NN} has the geometrical meaning that the larger the value of O_{NN} , the higher the degree of mixing in the cluster. Figure 6 shows clearly an increase in mixing of the two species of atoms in the clusters as n declines from 37 and the degree of mixing attains a maximum around $n \approx 22$. At $n=17$ we observe an abrupt drop in O_{NN} , implying that the cluster shifts from a well-mixed geometry to one displaying segregation with Cu atoms residing at the cluster center. As a result, C_n shows an entirely different structure from those in the first category. There are two common features for the nanoclusters in this

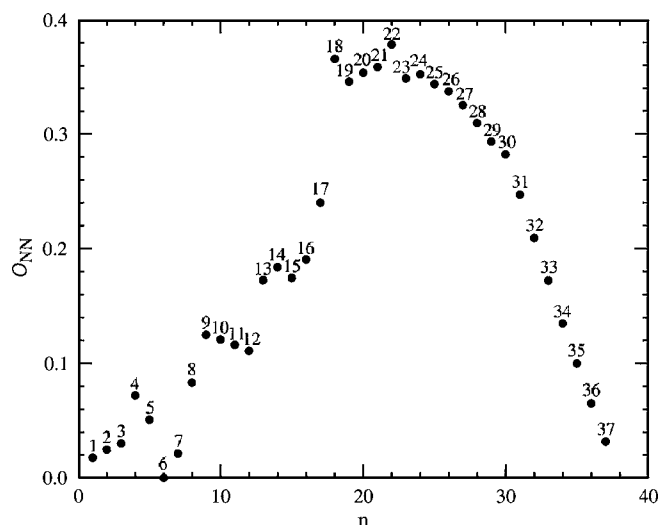


FIG. 6. Order parameter O_{NN} vs n (atom fraction of Cu) giving number of Au–Cu nearest-neighbor interactions relative to the total number of nearest-neighbor interactions. The numeric value on top of each solid circle refers to n of cluster C_n . Notice that the cluster C_6 has the smallest value, implying that it is least mixed.

category that can be visualized. The first one is that they *disfavor* quasispherical structure and prefer instead some kind of a stratified pancake structure. The second one is the change in structure from the *octahedral* to *pentagonal* geometry [compare, for example, C_{18} in Fig. 2(b) and C_{17} in Fig. 2(c)]. Let us describe how clusters in this category vary with n . Consider C_{17} , this cluster takes on a capped pentagonal shape (Cu is the vertex atom bonded to five Au atoms) if viewed from one side, but an indented pentagonal structure (the indented atom is Au bonded to five Cu atoms) if viewed from the directly opposite side. Sandwiched between the capped and indented pentagonal geometries are two atomic rings consisting each of ten atoms (the Cu and Au atoms

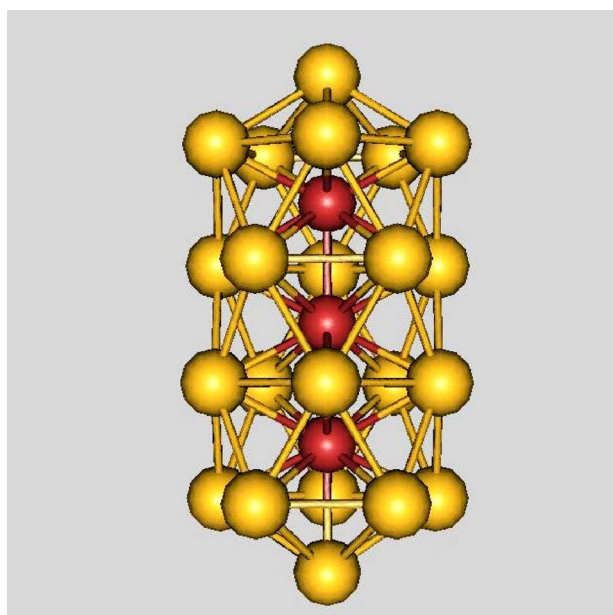


FIG. 7. (Color online) Lowest-lying isomer for Cu_3Au_{22} obtained by the PTMBHGA. This geometry is drastically different from that reported by Lordeiro *et al.* [shown in Fig. 4 of Ref. 14]. Red: Cu and Yellow: Au.

occupy alternate sites in the third layer, whereas the fourth layer consists of all Au atoms). Note furthermore that there is a pentagonal pyramid of Cu atoms embedded inside the cluster [see Fig. 2(c) for C_{17}]. At $n=16$, the structure changes by exchanging two Au atoms in the pentagonal sites (second layer), one with the capped Cu atom and another with the Cu atom originally in the third-layer ring. Then the additional Au atom is arranged to substitute for a Cu atom in the third-layer ring thus disrupting the regular alternate arrangement of the Cu and Au atoms. The next cluster C_{15} forms by merely removing a Cu atom in the third-layer ring and replacing it with the Au atom. It is interesting to note that a similar structural evolution is followed by the nanocluster C_{14} , which also displays the top-bottom pentagonal pyramids, but the capped pentagonal geometry and the pentagonal indentation are just the reverse of C_{17} . In other words, the capped (indented) atom is now the Au (Cu) atom bonded to the bottom (top) five Cu (Au) atoms. For C_{14} , two Au atoms originally in the fourth-layer ring of C_{15} have exchanged their sites with two Cu atoms in the second-layer pentagon, and the Cu atom to be substituted is in the third layer [see C_{15} in Fig. 2(c)]. With respect to C_{14} , the next atom fraction $n=13$ forms by substituting a Cu atom in the second layer with the Au atom as shown in Fig. 2(c).

Beginning at $n \leq 12$, the lowest-energy structure of C_n follows a totally different pathway. Generally one finds a switch in structure from the *pentagonal* to *hexagonal* symmetry [compare, for instance, C_{13} in Fig. 2(c) and C_{12} in Fig. 2(d)]. A simple way to understand the n dependence of $C_{4 \leq n \leq 12}$ is to focus on the distribution pattern of Cu atoms, for these atoms, being smaller in size, play the important role of an “inland” backbone that segregates them from the Au atoms. Figure 2(d) details the sites of Cu atoms in C_{12} . Well inside the cluster, six Cu atoms join to assume a hexagonal ring. On one side of the hexagonal plane, it is readily seen that three Cu atoms combine with three lateral *sides* of the hexagon resulting in three triangular faces each of which tilts at an acute angle away from the normal plane. On the opposite side, three Cu atoms at three alternate sites of the hexagonal face are associated with three Cu atoms forming three “open arms” [see Fig. 2(d)]. For C_{12} , the 26 Au atoms are positioned so that seven of them take on an indented hexagonal pyramid sitting on top of the hexagonal plane on the side with three Cu–Cu arms, and on the directly opposite side, three Au atoms alternate with the three Cu atoms of the triangular faces building another depressed hexagonal pyramid with a Au as the depressed atom. The remaining 15 Au atoms together with the three open-armed Cu atoms occupy sites that form the face-centered rectangular faces attaching one another and circling the central belt region. The next two clusters C_{11} and C_{10} are obtained by removing the armed Cu atoms, one at a time, and replacing them by Au atoms. This replacement continues until all three open-armed Cu atoms have been substituted by the Au atoms, and we arrive at C_9 characterized by three triangular faces attaching to the hexagonal ring [Fig. 2(d)]. It is anticipated that the next n variation of $C_{6 \leq n \leq 8}$ consists of one-at-a-time exchange of Cu by Au for those Cu atoms located at the triangular vertices. Breaking of the hexagonal ring begins at C_5 and terminates

TABLE II. Lowest-energy minima for bimetallic clusters Cu–Au.

n_{Cu}	n_{Au}	E (eV)	n_{Cu}	n_{Au}	E (eV)	n_{Cu}	n_{Au}	E (eV)	n_{Cu}	n_{Au}	E (eV)
0	38	–130.540 017	10	28	–128.441 113	20	18	–122.341 253	30	8	–115.532 589
1	37	–130.501 459	11	27	–127.829 980	21	17	–121.651 584	31	7	–114.691 322
2	36	–130.581 003	12	26	–127.210 768	22	16	–120.987 720	32	6	–113.859 947
3	35	–130.528 619	13	25	–126.592 550	23	15	–120.299 954	33	5	–113.031 935
4	34	–130.541 297	14	24	–125.987 628	24	14	–119.641 524	34	4	–112.213 997
5	33	–130.649 051	15	23	–125.394 566	25	13	–118.963 228	35	3	–111.390 551
6	32	–130.799 948	16	22	–124.820 135	26	12	–118.306 319	36	2	–110.577 204
7	31	–130.210 232	17	21	–124.234 811	27	11	–117.603 336	37	1	–109.767 291
8	30	–129.623 966	18	20	–123.702 295	28	10	–116.919 003	38	0	–108.967 590
9	29	–129.050 352	19	19	–122.991 483	29	9	–116.213 171			

at $n=4$ after which $C_{1 \leq n \leq 3}$ undergo a drastic change to disordered structures. Perhaps most exceptional is the bimetallic cluster C_6 [Fig. 2(d)]. This cluster assumes a distinctly lowest-energy value and hence is the most stable bimetallic cluster in $C_{1 \leq n \leq 37}$. Geometrically, we see the Cu atoms in C_6 forming a plane hexagon, centrally located with the Au atoms defining the cluster surface. This scenario is consistent with the results of $\langle R_{\text{Cu}} \rangle$ and ΔE_{mix} .

Finally, we come to the third category comprising the atom fraction of Cu from C_3 to C_1 . Figure 2(e) shows that these bimetallic clusters display amorphous structures. Here, the number of Au atoms predominates and the predicted global energy minimum of C_n changes irregularly with n . It can be seen that the Cu atom in C_1 buries inside the cluster of Au atoms trying to maximize the bond number, but the increase in internal strain ($r_{\text{Cu–Au}}=2.5259$ Å) has weakened the stability. In contrast, the two Cu atoms in C_2 are more successful in achieving both stability criteria, namely, the maximization of bond number and the reduction of the internal strain ($r_{\text{Cu–Au}} \approx 2.5466$ Å for a nearest-neighbor Au atom at a surface site; $r_{\text{Cu–Au}} \approx 2.5415$ Å for a nearest-neighbor Au atom at an internal site; $r_{\text{Cu–Cu}}=3.1083$ Å). This finding explains why C_2 has a lower energy than the pure Au cluster. The cluster C_3 that lies in between the above two cases deserves notice. This cluster is actually a synthesis of a double icosahedral geometry (with two Cu atoms sitting at the centers) and a disordered structure as shown explicitly in Fig. 2(f).

B. Comparison with theoretical, computer-simulated, and experimental studies

Both the theoretical calculations applying GA (Refs. 12, 14, and 15) and the computer simulation using molecular dynamics¹¹ have been reported for similar studies of Cu–Au. As concrete examples to check the reliability and stability of the PTMBHGA, we have chosen for comparison two recent GA calculations, one from Lordeiro *et al.*¹⁴ for Cu_xAu_y , $x+y \leq 30$ [Table III in Ref. 14] and the other from Rapallo *et al.*¹⁵ for Cu–Au of nuclearity $m=38$. The comparison with the Cu_xAu_y results of Lordeiro *et al.* is encouraging, for their lowest-energy values are all reproduced except for that of $\text{Cu}_3\text{Au}_{22}$. For this cluster, Lordeiro *et al.* determined the lowest-energy value to be -3.39584 eV, which is higher

than ours, -3.3964408 eV. This small difference in energy has resulted in an entirely different structure (compare Fig. 7 here and Fig. 4 in Ref. 14). Due to the lack of detailed numerical values, the same structural comparison with Rapallo *et al.*¹⁵ is less quantitative. However, for one of the clusters, $\text{Au}_{34}\text{Cu}_4$, where the geometry is depicted in Fig. 9 of Ref. 15, its calculated value is available.³² The predicted value is -130.4913 , much higher than ours (see Table II). To proceed to a more systematic comparison, we turn to investigate nanoclusters $\text{Cu}_n\text{Au}_{m-n}$ of lower nuclearities $m=13, 14$, and 19 . First of all, let us compare the lowest-energy structures of pure clusters. For Au_n , they are icosahedral for Au_{13} , amorphous for Au_{14} and Au_{19} , and truncated octahedral for Au_{38} ; whereas for Cu_{13} , Cu_{14} , Cu_{19} , and Cu_{38} , they take on icosahedral, icosahedral-based, double icosahedral, and truncated octahedral geometries, respectively. A comparison of the structural change of C_n with n and the three classes of bimetallic clusters^{12,14} reveals two interesting features. The first feature is that for the three bimetallic clusters with lower nuclearities, their structural changes with n proceed by preserving the icosahedral symmetry manifesting the mixing tendency of Cu and Au atoms (permutational isomers). This is in contrast to what is seen in C_n , where it undergoes segregation with the larger-sized Au atoms showing a preference to occupy sites on the surface relative to Cu atoms, which show a tendency to reside inside the core region. The same scenario was observed by Wilton and Johnston¹³ in their studies of Cu–Au nanoalloys of much larger nuclearity ($m>300$). Coming to the second feature, we find that there exists a range of n below which the values E_n of the nanoalloys stay nearly the same and after which E_n increases monotonously. A general trend for the nearly constant energy range with n can be deduced if we scrutinize the E_n vs n for C_n as well as those of $m=13, 14$, and 19 . It is readily seen from Fig. 1(a) that the extent of the Cu-poor region increases with increasing nuclearity m .

Relatively speaking it is more difficult to make a quantitative comparison between the present results and the experimentally observed nanoclusters because most experiments on these composite materials are directed at nanoalloys of much larger size and obtained usually in the presence of substrates. For the specific case of Cu–Au, early^{18,19} and more recent^{17,20–22} experiments have been reported using various techniques, e.g., transmission electron microscopy, energy dispersive x ray, low-energy ion scatter-

ing or x-ray photoemission spectroscopy, extended x-ray absorption fine structure spectroscopy, etc., to investigate the structure and composition of nanoalloys. Among them, Wilson and Johnston¹³ have given a detailed description of some of these experimental works (Refs. 17 and 19) and, from comparing theoretical calculations and measurements, commented on the possible reasons for the discrepancies. Many of the factors pointed out there between the theoretical and experimental findings apply to our present results also. We shall not therefore delve further into this issue. We should mention, however, one exceptional aspect. In the present work, we have predicted the lowest-energy isomers for both pure clusters Cu_{38} and Au_{38} to be the truncated octahedron. In our case, this truncated octahedral geometry spans over the range of $38 \leq n \leq 18$ with C_n appearing as permutational isomers. It is perhaps worthwhile to note furthermore that despite incompatibility with the face-centered cubic structure observed by Pauwels *et al.*¹⁷ in their electron diffraction and high-resolution electron microscopy experiments, our prediction of the segregation behavior for $\text{Cu}_{29}\text{Au}_9$ agrees roughly with their Monte Carlo simulation for the free clusters $(\text{Cu}_3\text{Au})_M$ ($M=113.5$ and 196.5), where their simulation results indicate Au deficiency in the core and that the Au atoms are rich in the mantle.

IV. CONCLUSION

We summarize four main findings using the present method.

- (1) We worked on the transformed PES having staircase topography. As a result, the usual potential-energy barriers have been replaced by some "large-scaled truncated barriers." In conjunction with the idea of imposing "MC machines" and the use of the multicanonical weight factors and PT, the scope of geometrical searching path increases, making the usual searching for the lowest-energy minimum that involves the dynamic jump over the large-scaled truncated barrier much easier.
- (2) Treating the MC machines as parents in GA is a novel idea and is more predictive than the usual randomly generated parents. The CPU resources can be used efficiently if the code is programmed in a parallel-distributed environment. With the optimistic view of foreseeing better performance for personal computers, the amount of computing time needed for investigating larger clusters will be technically reduced, and a theoretical study of the latter becomes promising.
- (3) The structural properties of the atom-fraction dependence of the bimetallic clusters Cu–Au can be understood in terms of three well-defined categories. The first category $C_{18 \leq n \leq 37}$ is characterized by C_n favoring the quasispherical geometry with Au atoms occupying surface sites. Octahedral symmetry is the common scenario. The second category $C_{4 \leq n \leq 17}$ is described by the stratified pancake structure. Bimetallic clusters in this category prefer pentagonal (for $C_{13 \leq n \leq 17}$) and hexagonal (for $C_{4 \leq n \leq 12}$) symmetries. Finally in the third cat-

egory $C_{1 \leq n \leq 3}$ for which Au atoms are predominant, C_n is characterized by disordered structures.

- (4) The atom-fraction n dependence of C_n differs from those nanoalloys of lower nuclearities by its stronger effect. Together with the E_n vs n of nuclearities $m=13, 14$, and 19 , we deduce that the extent of the nearly constant energy range of n in the Cu-poor region increases with nuclearity.

We finally note in passing that the present optimization algorithm is not limited to the study of nanoparticles only. The algorithm should be useful for other physical problems as well. It can be used, for instance, in the prediction of protein folding structures.

ACKNOWLEDGMENT

We acknowledge the financial support (Grant No. NSC93-2112-M-008-035) from the National Science Council, Taiwan, Republic of China.

¹D. M. Deaven and K. M. Ho, Phys. Rev. Lett. **75**, 288 (1995).

²Y. Zeiri, Comput. Phys. Commun. **103**, 28 (1997).

³C. Roberts, R. L. Johnston, and N. T. Wilson, Theor. Chem. Acc. **104**, 123 (2000).

⁴R. L. Johnston, J. Chem. Soc. Dalton Trans. **22**, 4193 (2003) and references cited therein.

⁵D. J. Wales and J. P. K. Doye, J. Phys. Chem. A **101**, 5111 (1997).

⁶Z. Li and H. A. Scheraga, Proc. Natl. Acad. Sci. U.S.A. **84**, 6611 (1987).

⁷J. P. Neirotti, F. Calvo, D. L. Freeman, and J. D. Doll, J. Chem. Phys. **112**, 10340 (2002).

⁸N. Rathore, M. Chopra, and J. J. de Pablo, J. Chem. Phys. **122**, 024111 (2005).

⁹C. Maurizio, G. Mattei, P. Mazzoldi, S. Padovani, E. Cattaruzza, F. Gonella, F. D'Acapito, and F. Zontone, Nucl. Instrum. Methods Phys. Res. B **200**, 178 (2000).

¹⁰G. Rossi, A. Rapallo, C. Mottet, A. Fortunelli, F. Baletto, and R. Ferrando, Phys. Rev. Lett. **93**, 105503 (2004).

¹¹M. J. López, P. A. Marcos, and J. A. Alonso, J. Chem. Phys. **104**, 1056 (1996).

¹²S. Darby, T. V. Mortimer-Jones, R. L. Johnston, and C. Roberts, J. Chem. Phys. **116**, 1536 (2002).

¹³N. T. Wilson and R. L. Johnston, J. Mater. Chem. **12**, 2913 (2002).

¹⁴R. A. Lordeiro, F. F. Guimarães, J. C. Belchior, and R. L. Johnston, Int. J. Quantum Chem. **95**, 112 (2003).

¹⁵A. Rapallo, G. Rossi, R. Ferrando, A. Fortunelli, B. C. Curley, L. D. Lloyd, G. M. Tarbuck, and R. L. Johnston, J. Chem. Phys. **122**, 194308 (2005).

¹⁶J. L. Rodríguez-López, J. M. Montejano-Carrizales, and M. José-Yacamán, Appl. Surf. Sci. **219**, 56 (2003).

¹⁷B. Pauwels, G. Van Tendeloo, E. Zhurkin, and M. Hou, Phys. Rev. B **63**, 165406-1 (2001).

¹⁸G. Meitzner, G. H. Via, F. W. Lytle, and J. H. Sinfelt, J. Chem. Phys. **83**, 4793 (1985).

¹⁹H. Yasuda, H. Mori, M. Komatsu, and K. Takeda, J. Appl. Phys. **73**, 1100 (1993).

²⁰W. Bouwen, F. Vanhoutte, F. Despa, S. Bouckaert, S. Neukermans, L. T. Kuhn, H. Weidele, P. Liewens, and R. E. Silverans, Chem. Phys. Lett. **314**, 227 (1999).

²¹K. Akamatsu, T. Kawamura, H. Nabika, S. Deki, T. Strunskus, and F. Faupel, J. Mater. Chem. **12**, 3610 (2002).

²²C. Maurizio, G. Mattei, P. Mazzoldi, S. Padovani, E. Cattaruzza, F. Gonella, F. D'Acapito, and F. Zontone, Nucl. Instrum. Methods Phys. Res. B **200**, 178 (2003); C. Maurizio, F. Gonella, E. Cattaruzza, P. Mazzoldi, and F. D'Acapito, *ibid.* **200**, 126 (2003).

²³F. Cleri and V. Rosato, Phys. Rev. B **48**, 22 (1993).

²⁴C. H. Chien, E. Blaisten-Barojas, and M. R. Pederson, J. Chem. Phys. **112**, 2301 (2000).

²⁵M. J. López and J. Jellinek, J. Chem. Phys. **110**, 8899 (1999).

²⁶R. P. Gupta, Phys. Rev. B **23**, 6265 (1981).

²⁷F. Belatto and R. Ferrando, *Rev. Mod. Phys.* **77**, 371 (2005).

²⁸L. Zhan, B. Piwowar, W. K. Liu, P. J. Hsu, S. K. Lai, and J. Z. Y. Chen, *J. Chem. Phys.* **120**, 5536 (2004).

²⁹S. K. Lai, P. J. Hsu, K. L. Wu, W. K. Liu, and M. Iwamatsu, *J. Chem. Phys.* **117**, 10715 (2002).

³⁰A relevant discussion on the choice of an optimal schedule values of β_i^{PT} has been given by Kone and Kofke [A. Kone and D. A. Kofke, *J. Chem. Phys.* **122**, 206101 (2005)] in a recent short report. Here we have considered as a reference the value $\beta_i^{\text{PT}}=1.25$ previously used by Wales and Doye (Ref. 5) in their study of the Lennard-Jones system. Our experience with different metallic clusters tested with β_i^{PT} varying on both sides of $\beta_i^{\text{PT}}=1.25$ suggests that an *increase* in magnitude of the β_i^{PT} from 1.25 works well generally.

³¹It should be pointed out here that the number of steps used in each of these recursive processes was merely a guide to numerical work. Depend-

ing on the cluster size and type (pure or bimetallic cluster), these numbers of steps can always be adjusted from these suggested values. The ones given here were checked by us to be sufficient for the present purpose and, for pure metallic clusters, a size up to around 300 has been attempted also.

³²This value is kindly supplied to us by Dr. R. Ferrando (private communication). As further illustration, we have in fact compared the lowest-energy values of two more clusters, $\text{Ag}_{37}\text{Cu}_1$ and $\text{Ag}_1\text{Cu}_{37}$, which were reported also in the same paper. For these clusters, the PTMBHGA yields $-97.671\,190$ and $-113.242\,280$ eV, respectively, which are again lower than those values -97.5985 and -113.0296 eV obtained by Rapallo *et al.* (Ref. 15) using the same set of Gupta potential parameters [Table II of Ref. 15] in the simulated annealing and genetic algorithm technique. More quantitative results for Ag–Cu will be reported elsewhere.